ト系ステンレス鋼 SUS316 である．その試験片形状を Fig. 3 に示す．ここで，軸力の中心とリガメント中心を一致させ，軸力による曲げモーメントの発生を抑えた．リガメント部には自作した光塑性皮膜を取り付けた．

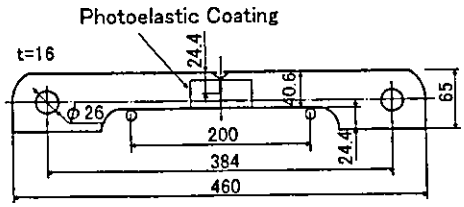

Fig.3 Geometries figure of the specimen

3.2 負荷条件

負荷履歴として，3 つの試験パターンで実験を行った．
①軸力・曲げを同時に負荷．　(同時負荷試験)
②軸力を負荷後，曲げを負荷．　(軸力→曲げ試験)
③曲げを負荷後，軸力を負荷．　(曲げ→軸力試験)
各試験パターンの負荷経路を崩壊限度線図上に示し，限度曲線全域で通過するよう軸力および曲げ一定値を設定した．

4. 実験結果および考察

4.1 光塑性皮膜法による崩壊点判定

Fig. 4 は，光塑性縞の一縞目 (0.2%耐力にほぼ一致) がリガメント部を貫通した時点の観察結果である．すべり線の進展経路の違いから，負荷形態により塑性域の進展は大きく異なることがわかる．いずれも切欠先端から縞が発生するが，軸力の影響が強い試験では，軸線に対しほぼ 45 度の方向で進展し下端で貫通する．曲げの影響が強い試験では，下端からも進展しリガメント中央で貫通する．同時負荷試験では，上 2 つの中間の形といえる．このように，塑性域が試験片全幅を貫通する様子をはっきり捉えることができる．

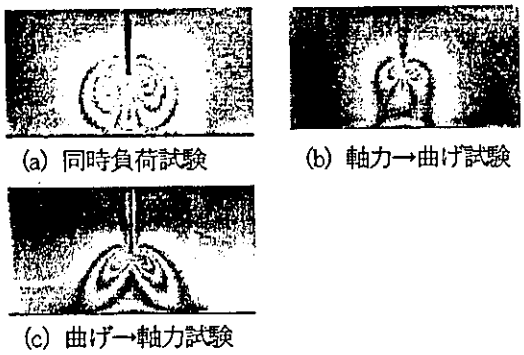

(a) 同時負荷試験　(b) 軸力→曲げ試験

(c) 曲げ→軸力試験

Fig.4 Observation of the ligament.

4.2 負荷履歴が塑性崩壊荷重に及ぼす影響の評価

3 つの試験パターンについて，光塑性皮膜法で判定した崩壊点を崩壊限度線図上にプロットしたものを Fig. 5 に示す．同時負荷試験を●，軸力→曲げ試験を▲，曲げ→軸力試験を■で表す．

崩壊点は上界曲線に沿うように分布し，試験パターンによって大きく外れる点もないことから，負荷履歴による影響は見られない．また，供試材料の降伏応力を基準にとった理論曲線は，安全側の値を示した．

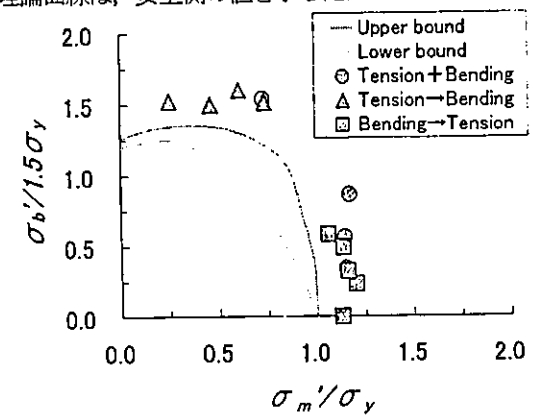

Fig.5 The distribution of the plastic collapse point

4.3 荷重ー変位線図による崩壊点判定法の評価

Fig. 6 に，試験で得られた膜応力強さー縦ひずみ線図 (○)，曲げ応力強さーたわみ角線図 (△)，一次応力強さー切欠先端開口変位線図 (□) より，二倍変位法を使って求めた崩壊点を崩壊限度線図上に示す．◆で示すのは，比較基準として光塑性皮膜法で判定した崩壊点である．二倍変位法の他の方法でも求めて検討した結果，二倍変位法が最も近い値を示した．

線図別に比較すると，全域に渡り理論曲線に非常に近い分布を示したのは，一次応力強さー切欠先端開口変位線図より判定した結果であった．曲げ応力強さーたわみ角線図の場合には，膜応力成分の影響が大きな試験条件では精度に欠ける結果となった．膜応力強さー縦ひずみ線図については，分布にばらつきがあり曲げの大きい試験では適用できないため，今回の結果からは崩壊点判定に不適であると判断される．

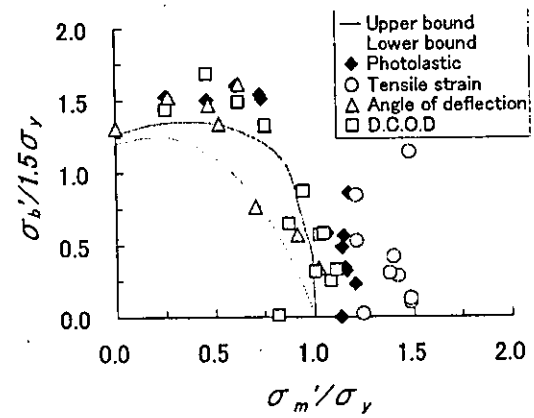

Fig.6 The distribution of the plastic collapse point.

参 考 文 献

(1) Green, A. P, J. Mech. Phys & Solids, 4-3(1965), 259-268

(2) Rice. J. R., Proceedings of Surface Flaw Symposium, ASME Winter Annual Meeting, (1972-11)

(3) 岡村・高畑・影山,機論, 49-455A (1979), 1076-1081

PVP-Vol. 443-2, Fatigue, Fracture, and Damage Analysis — 2002
Volume II
ASME 2002

PVP2002-1355

LOAD HISTORY EFFECT ON PLASTIC COLLAPSE IN A SINGLE-EDGE NOTCHED SUS316 SUBJECTED TO A COMBINED TENSION AND BENDING

Satoru Izawa[1], Masaaki Matsubara[2], Kikuo Nezu, Kenji Sakamoto

[1]Oyama National College of Technology, 1467-2, Nakakuki, Oyama, Tochigi, Japan
tel (+81)285-20-2211 fax(+81)285-20-2884, izawa@oyama-ct.ac.jp
[2]Gunma University, 1-5-1, Tenjin-cho, Kiryu, Gunma, Japan
tel(+81)277-30-1536 fax(+81)277-30-1539,matsubar@ me.gunma-u.ac.jp
tel(+81)277-30-1535 fax(+81)277-30-1599, nezu@me.gunma-u.ac.jp
tel(+81)277-30-1537 fax(+81)277-30-1599, sakamoto@ me.gunma-u.ac.jp

ABSTRACT

This paper is evaluates the effects of load history on the plastic collapse load of stainless steel members with a single-edge notch. It considers, both the tension force due to an internal pressure and the bending moment caused by an earthquake, considered as load cases for a structure. Experimental equipment was specially developed to cope with the indeterminate problems in fracture mechanics. In this experiment, the stress state of a plastic collapse point was assessed using a membrane stress and axial displacement chart as well as a bending stress and deflection angle chart, which is well known as the ligament method. As a result, we successfully developed a new method for assessing plastic collapse under a complex load. We found that a different load history affects the formation of the plastic region and the collapse point position. The effects of load history on the plastic collapse load were not very big.

INTRODUCTION

The destruction of stainless steel equipment used for light water plants may cause crucial social problems. Structural engineers seek to prevent such problems by guaranteeing a sufficient margin for the fracture strength based on the existence of assumed defects. In recent years, extending the life of the power-plant equipments has been the urgent problems, especially as a Japanese national project [1] [2]. The physical phenomena improving of the safety margin are discussed below.

In operating piping systems, the bending moments due to earthquakes and axial forces due to internal pressures are considered to be factors contributing to the destruction of plants. Few papers have examined the effect of the load hysterisis on the plastic collapse under compound loading of axial forces and bending moments. In real situations, the large safety margins have been provided eliminate plastic collapse.

This paper develops the experimental system in which the axial force and the bending moment can be controlled independently in order to study indeterministic fracture mechanics [3]. Using this system, we successfully explored the effect of load hysterisis on the plastic collapse point of SUS316 steel with a notch. This study is explained explained using a plastic collapse limit chart.

NOTATION

a	notch depth
W'	width of ligament
W	width of specimen
B	thickness
F	axial force
M	bending moment
P_m'	membrane stress intensity
P_b'	bending stress intensity
σ_y	yield stress (0.2% proof stress)
σ_B	tensile strength
λ	axial displacement
θ	angle of deflection
ε_1	principal strain
N	fringe order
β	sensitivity of the photo elastic strain
t	width of the photo elastic coating
ν	Poisson ratio
ε_o	reference strain
σ_o	reference stress

ANALYSIS

Plastic collapse load

The specimen geometry is shown Fig. 1. The centerline of the axial force was set coincident with that of the ligament in order to suppress the bending moment M generated by the axial force F. The membrane stress intensity P_m' and bending stress intensity P_b' are given by the following.

$$\left.\begin{aligned} P_m' &= F/BW' \\ P_b' &= 6M/BW'^2 \end{aligned}\right\} \cdots\cdots\cdots(1)$$

where W' is width of the ligament.

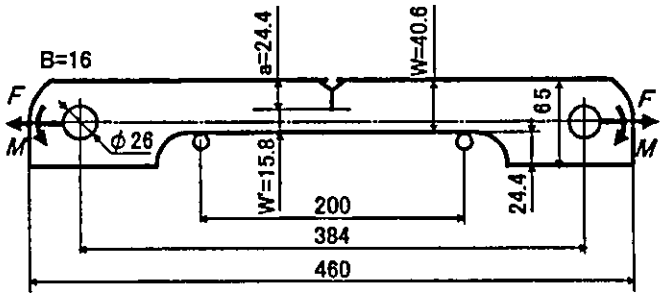

Fig. 1 Geometries of the specimen

Ductile materials plants are usually designed based on the plastic collapse limit. The horizontal axis of collapse limit curve is obtained by dividing the membrane stress intensity P_m' obtained from the tension test of the notched specimen, by yield stress σy for non-notched material. The vertical axis of collapse limit curve shows bending stress intensity P_b' divided by 1.5 times the yield stress σ_y.

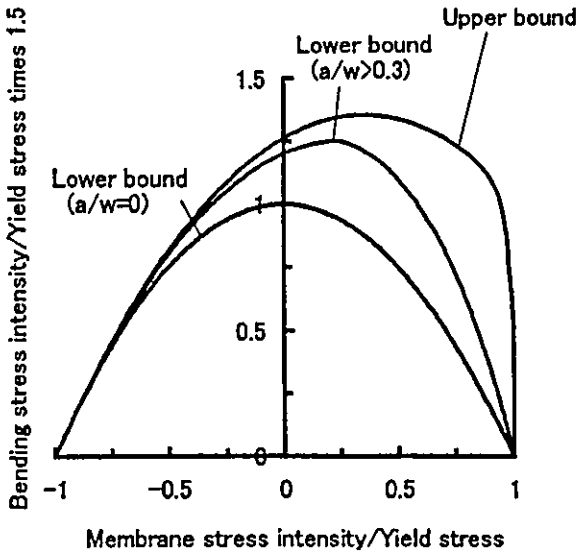

Fig. 2 Collapse limit curve

$$\frac{P_b'}{1.5\sigma_y} = 1 - \left(\frac{P_m'}{\sigma_y}\right)^2 \cdots\cdots\cdots(2)$$

The collapse load of a unilaterally notched material with optional notch depth is the collapse load that the rigid perfect plasticity body is subjected to by an axial force and the bending moment. The result upper bound is obtained by the dynamically capasitable slip line field by Rice and the solution of pure bending in a slip-line field by Green. The lower bound is obtained from the correction of notch effects by Okamura, Kageyama and Takahata. [4] [5] [6] [7].

EXPERIMENTAL METHOD

Test equipment and testing

Figure 3 shows the test equipment and actual testing, in which bi-horizontal and vertical loads can be controlled independently. The displacements, loads in horizontal and vertical directions, angles of deflection and notch opening displacement are measured. The material used is austenitic stainless steel SUS316 (Japanese Industrial Standard).

The mechanical properties of tested materials are listed in Table 1.

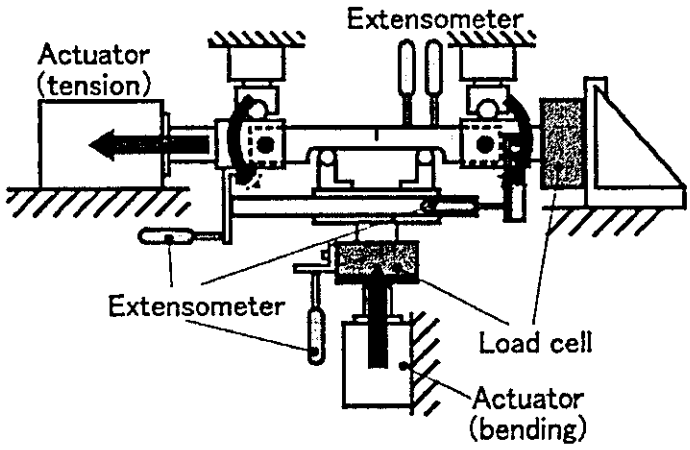

Fig. 3 Schematic illustration of testing equipment

Table 1 Mechanical properties of tested materials

Material	Yield stress σ_y[MPa]	Tensile strength σ_B[MPa]	Elongation [%]
SUS316	272	553	56

Load conditions

The experiment was carried out in the three test cases shown, in Fig. 4.

Load condition ①···Pattern (Tension + Bending)
Axial force and bending simultaneous load test.

Load condition ②···Pattern (Tension → Bending)
Axial force after bending test.

Load condition ③···Pattern(Bending → Tension)
Bending after axial force test.

In Fig.4, the lower bound of the axial force under bending load with no notch is considered to be the standard reference (Lower bound *a/W=0*). The bending moment and axial force were selected have been selected based on the collapse limit curve. Table 2 shows goal load of the collapse load. The effect of the load history on collapse load was clarified by the coupling collapse points obtained in our experiments.

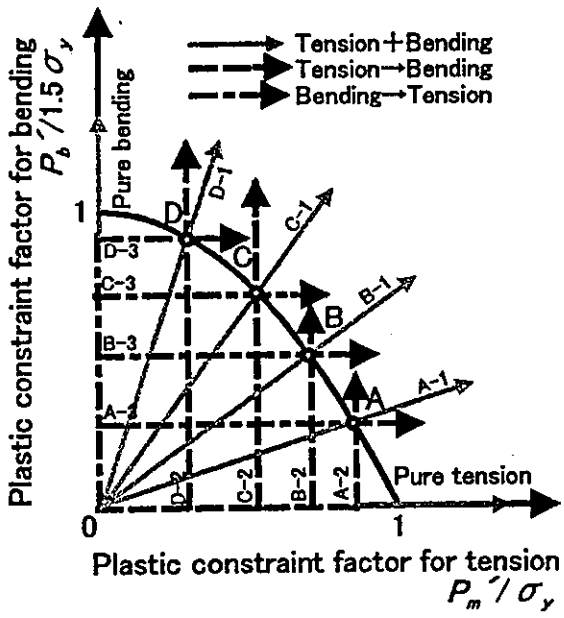

Fig. 4 Loading path on the plastics collapse diagram

Table 2 Goal load of the collapse point

Load point	Pb'/Pm'
Pure tension	0
A	0.49
B	1.09
C	2.07
D	4.62
Pure bending	∞

Visualization of plastic collapse by the photo elastic coating method

We visualized the plastic region by the photoelastic coating method to observe the progress of the plastic region of the ligament, using a photo elasticity film made of cold setting epoxy resin in the observation. The photo elasticity film was bounded to the ligament portion so that we could examined the relationship between the collapse point and the stress behavior in the plastic region with the sensitivity of the photo elastic strain β is this experiment.

$$\beta = \frac{N}{2t(\varepsilon_1 - \varepsilon_2)} = 28(1/mm) \cdots\cdots\cdots (3)$$

where the principal strain difference $\varepsilon_1 - \varepsilon_2$ in equation (2) is given by

$$\varepsilon_1 - \varepsilon_2 = (1+\nu)\varepsilon_1 \cdots\cdots\cdots (4)$$

N in equation (2) is the fringe order in the axis tension test, and ν is the Poisson ratio. ν is set to 0.5 in the plastic region, and t is the width of the photo elastic coating.

Figure 5 shows a schematic illustration of the experiment. The observation of the photo elastic coating used the digital video camera. Mercury lamp was used for the light source. By reflecting in the specimen, the light of the mercury lamp was photographed in the digital video camera.

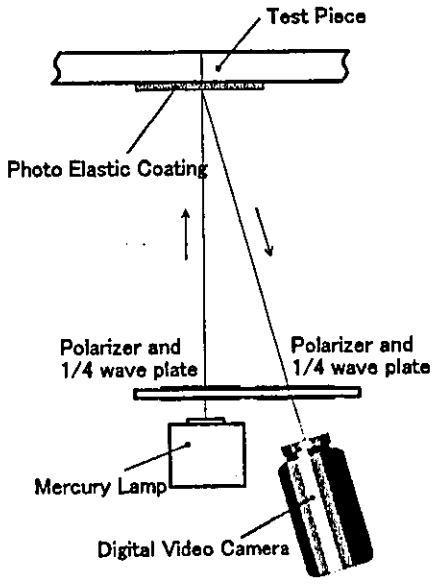

Fig. 5 Schematic illustration of the experiment

RESULT AND DISCUSSION

Deciding the collapse point

In this study, the collapse point is defined as the point at which the ligament plastic region penetrates the ligament part of the notched material at which deformation increases dramatically. To decide due to uniaxial stress, we used the charts shown in the following section based on the relation-ship between load and displacement. In so doing, we adopted the tangential method to decide the collapse point. In this method, the collapse point can be obtained from the intersection between the plastic deformation line and the elastic line as shown in Figs. 6 and 7.

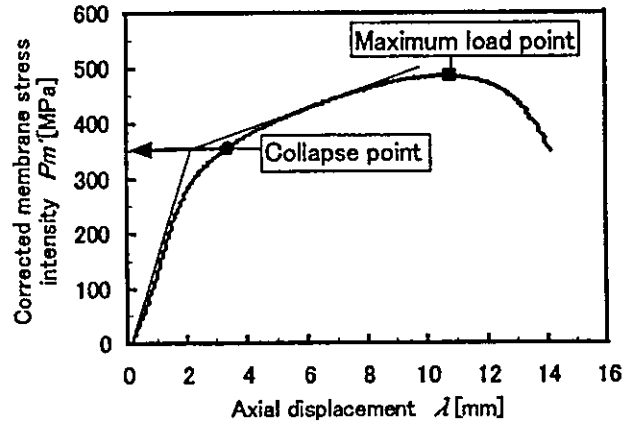

Fig. 6 Relationship between membrane stress and axial displacement chart

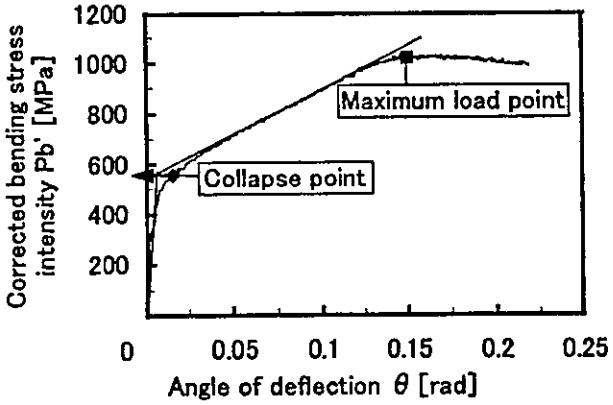

Fig. 7 Relationship between bending stress and rotation chart

Membrane stress intensity and axial displacement

Figure 6 shows the relationship between axial displacement λ and membrane stress intensity Pm'. Figure 5 can be applied for load conditions ① and ③ (axial force and bending moment test, bending moment after axial force test) because the membrane stress intensity is constant. However, Fig. 6 does not apply for load condition ② (axial force after bending moment test).

Bending stress intensity and angle of deflection

Figure 7 shows the relationship between the axial angle of deflection θ and bending stress intensity Pb'. It can be applied for load conditions ① and ② (axial force and bending moment test, axial force after bending moment test) because the membrane stress intensity is constant. However, Fig. 7 does not apply for load condition ② (bending moment after axial force test).

Evaluation by the collapse limit curve

Figure 8 shows the results of the distribution of collapse points. White symbols (○,◇, and □) indicate the results estimated by membrane stress; black symbols (●,◆, and ■) indicate the results estimated by bending stress.

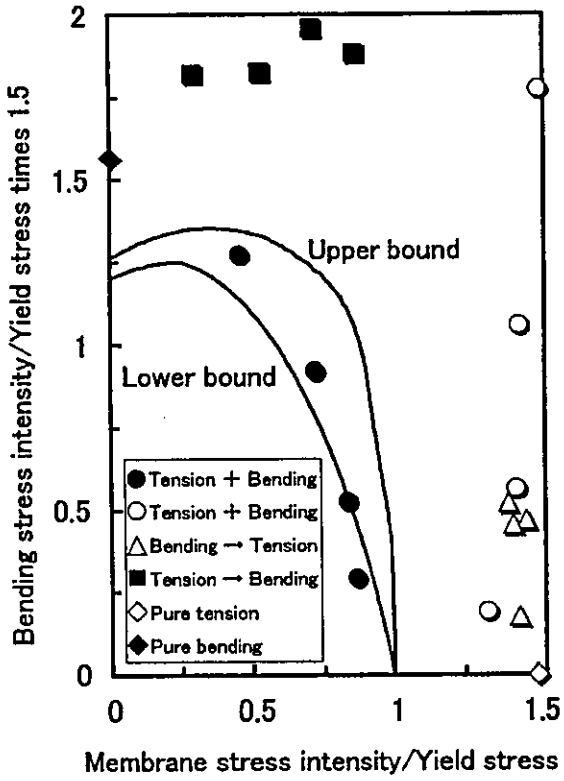

Fig. 8 Distribution of the plastic collapse point evaluating by chart

We found that the collapse points are distributed within the theoretical collapse load region, except for the case of tension and bending, which were estimated by bending stress (●), although the stress in the section exceeded the theoretical collapse load. We believe that materials with a relatively large work hardening

coefficient exhibit an excessive collapse load. The black dots, representing evaluation by bending in the case of in tension and bending distribute between the limit line obtained by the upper and lower bound theory In tension and bending tests (○, ●). It is possible to predict, collapse by using bending stress and membrane stress intensity.

The white triangles(bending → tension ; △) exhibit almost the same value as the white circles (tension → bending ; ○) on the horizontal axis Pm'/σ_y when the results were evaluated by membrane stress. The load hysteresis thus does not seem to affect the results in the evaluation by membrane stress. This results in the release of bending tension after bending.

Evaluation of the collapse limit curve using flow stress theory

As shown in Fig. 8, the plastic collapse points are distributed beyond the limit line because of the large work hardening coefficient of stainless steel Therefore, in Fig. 9 the authors adopted flow stress σ_f for estimating the plastic collapse load instead of yield stress σ_y.

$$\sigma_f = \frac{3\sigma_y + \sigma_B}{4} = 313[MPa] \cdots\cdots\cdots (5)$$

where σ_B is the Tensile strength.

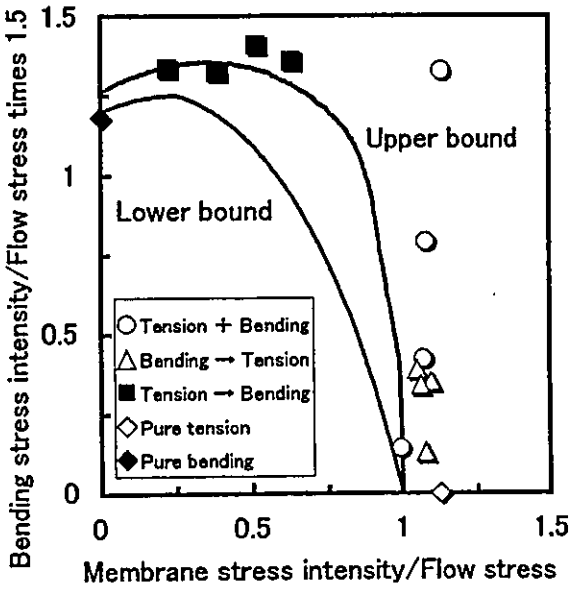

Fig. 9 Distribution of the plastic collapse point evaluating by flow stress

The distribution of the collapse points agrees well with the results of pure bending and pure tension. The work hardening coefficient n obtained by the Ramberg-Oswood rule is 5.1, and constant number α is 1.8.

$$\frac{\varepsilon}{\varepsilon_o} = \frac{\sigma}{\sigma_o} + \alpha\left(\frac{\sigma}{\sigma_o}\right)^n \cdots\cdots\cdots (6)$$

where σ_o is the reference stress, and ε_o is the reference strain.

Photo elastic coating method

Relationship between strain and fringe order

The relationship between stress, fringe order and strain difference is shown in Fig.10, where black dots indicate the plot of the principle stress, and black triangles, that of the strain difference. The fringe of the film is seen in the plastic region of the ligament. The first fringe was set to equals the yield point (0.2% proof stress) in the uniaxial tension test. The penetration point in the ligament of the first fringe that occurred in the top of the notch was defined as a collapse point.

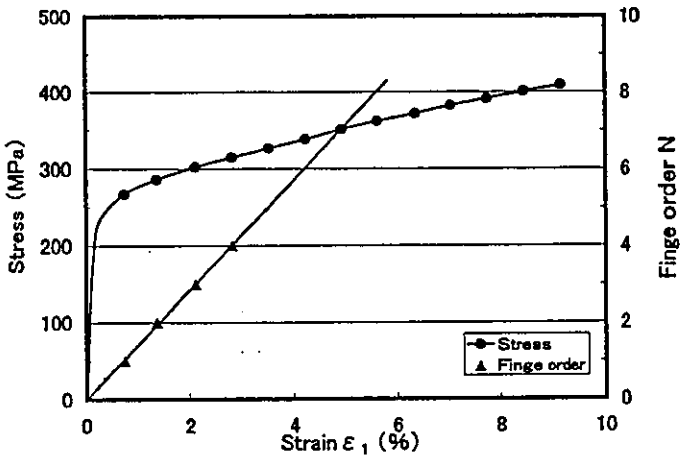

Fig. 10 Relationship between stress, fringe order and strain

Visualization of a ligament

The plastic region that evolves in the ligament differs greatly difference depending on load formation of the bending and tension. This difference of the evolution of the plastic region is considered to be due to the different formations of the slip line that directly affect the results of

plastic collapse in the ligament. Figure 11 shows a photograph of the ligament at the first stage when the first fringe reaches the ligament in the simultaneous test of tension and bending loads.

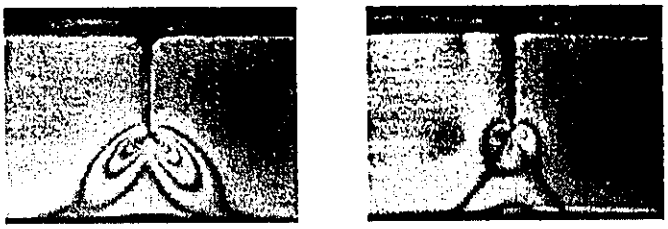

Pure tension Pure bending

Fig. 11 Photograph of the ligament

Figure 12 shows the schema of the slip line field of the ligament. Photoelasticity fringe and the slip line field of the schema showed the similar shape.

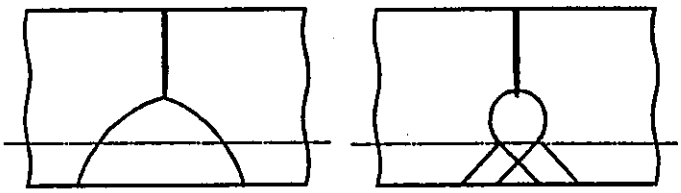

Pure tension Pure bending

Fig. 12 Schema of the slip line field of the ligament

Simultaneous test by tension and bending

Figure 13 shows a photograph of the simultaneous test of tension and bending loads. The fringe can occur in the top of the crack. However, compared with other load conditions, a higher fringe density can be produced due to the stagnation of the fringe penetration. In this case, bending is considered to be the dominant factor in the plastic collapse phenomenon.

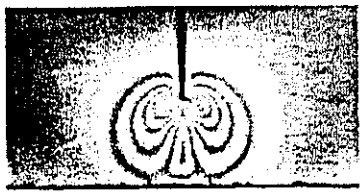

Fig. 13 Photograph of the simultaneous test

Bending after tension test

In this case, the tension force as an after load is the dominant factor in the plastic collapse. This is produced under each loading condition. When a slip line field that evolves which evolves in the top of the crack reaches the ligament, a fringe penetrates the plastic region due to the release of compressive force by bending in the free end of the test piece.

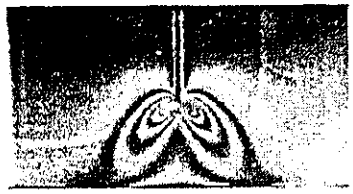

Fig. 14 Photograph of the bending after tension test

Tension after bending test

In this case, the bending as an after load is the dominant factor in the plastic collapse. We also observe that fringes occurring in both the bottom and the free end penetrate the central region of the ligament in Fig. 15. The radius of the circular arc, produced increases as the ratio of the tension to the bending increases, and the arc center moving toward the free end of the ligament portion.

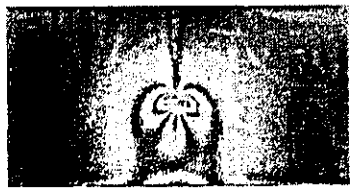

Fig. 15 Photograph of the tension after bending test

Distribution of the plastic collapse point

Membrane stress and bending stress as plastic region penetrated the ligament was calculated. Figure 16 shows the distribution of the plastic collapse point evaluating by the photo elastic coating method. The plastic collapse points are distributed beyond the limit line. The value of collapse point load evaluating by the photo elastic coating method smaller than that of the chart (Membrane stress intensity — axial displacement chart and Bending stress intensity — angle of deflection chart). Therefore, combined tension and bending load history does not affect the plastic collapse point.

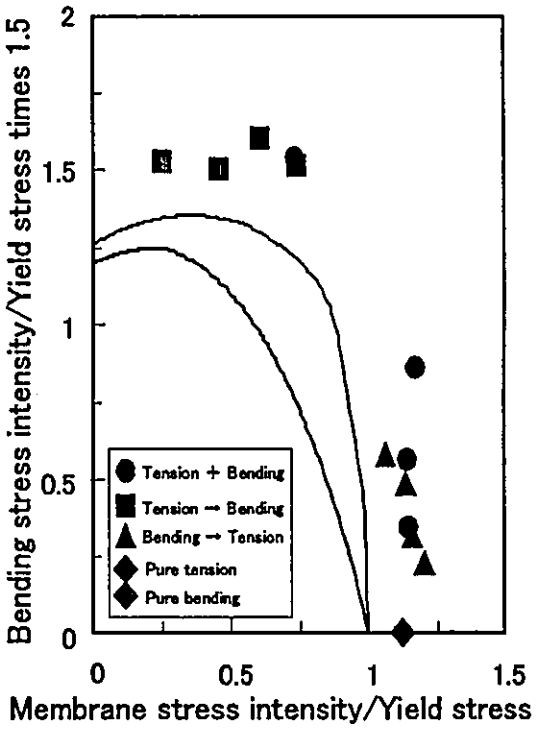

Fig. 16 Distribution of the plastic collapse point evaluating by the photo elastic coating method.

CONCLUSIONS

We examined the plastic collapse load of the notched stainless steel sample subjected to both tension and bending and experimentally clarified the effects of load history on the plastic collapse. Conclusions obtained are summarized bellow.

(1) The combined tension and bending load history does not affect the plastic collapse point. The collapse point determined by evaluating membrane stress in the simultaneous bending and tension tests could be misleading and dangerous.

(2) The flow stress rule can effectively predict the plastic collapse point in the collapse limit chart.

(3) We visualized the ligament by the photo elastic coating method to observe the formation of the plastic region. We found that the formation of the plastic region that penetrates the ligament of the notched stainless steel depends on the load history due to the different slip-line formations in the ligament caused by different load conditions.

REFERENCES

1. An , Ando, Ishiwatari & Hasegawa, Plastic Collapse Behavior of Pipes with Local Wall Thinning Subjected to bending Load and Allowable Limit. , JHPI, 36 - 4 (1998) , 33-41

2. Shiratori, Yakura, Ogasawara, Nakamura & Otani, Failure Analysis of Degraded Piping Against Seismic Loading, Trans. JSME (A), (2001-2), 209-215

3. Matsubara, Izawa, Hirao, Busujima, Koyama & Machida, Development of Testing Equipment for studying Statically Indeterminate Fracture Mechanics, Kawada, Sakamoto & Nez, Trans. JSME (A), (2001-7), 1218-1222

4. Green, A.P, The plastic yielding of shallow notched bars due to bending, J.Mech.Phys & Solids, 4-3(1965), 259-268

5. Rice.J.R., The line spring model for surface flows, in The Surface Crack: Physical Problems and Computational Solutions, Proceedings of Surface Flaw Symposium, ASME Winter Annual Meeting, (1972-11), 171-185

6. Okamura, Kageyama & Takahata, Lower bound solutions and their application to the collapse load of a cracked member under axial force and bending moment, Trans. JSME,, 49-455A (1979) , 1076-1081

7. A.G.Miller, Review of Limit Loads of Structures Containing Defects, Int. J. Pres. Ves. & Piping, 32, (1988), 197-327

論　文

光弾性皮膜法による軸力—曲げ複合荷重下のSUS316鋼片側切欠部材の塑性崩壊挙動

小山工業高等専門学校
伊澤　悟

群馬大学
松原雅昭

根津紀久雄
小山工業高等専門学校
橋本彰三

2004年3月号別刷
実験力学　Vol. 4　No. 1　pp.55～60.

日本実験力学会
The Japanese Society for Experimental Mechanics

論文

光弾性皮膜法による軸力一曲げ複合荷重下のSUS316鋼片側切欠部材の塑性崩壊挙動

伊澤 悟*, 松原 雅昭**, 根津紀久雄**, 橋本 彰三***

Plastic Collapse Behavior of a SUS316 Single-edge Notched Member Subjected to Combined Tension and Bending Using Photoelastic Coating Technique

Satoru IZAWA, Masaaki MATSUBARA, Kikuo NEZU and Shozo HASHIMOTO

The authors investigate plastic collapse patterns in a SUS316 single-edge notched member subjected to combined tension and bending using photoelastic coating technique. Conclusions are as follows:(1)The slip-line field of rigid-perfect plasticity body assumption which gives upper-bound solution is correspondent to the locus of the tip of plastic region which grows to the ligament direction in actual elastic-plastic material, (2)The plastic collapse pattern is almost decided in plotted position, when the collapsing load of the member is plotted on the plastic collapse limit diagram. The plastic collapse pattern is divided into three, Green, Rice and Hundy types and (3)From conclusion (1) and (2), the collapsing load of the member follows upper-bound solution regardless of load history.

Key words: Experimental Stress Analysis, Material Testing, Photoelastic Coating, Plastic Collapse, Slip Line Field, Notch, Combined Tension and Bending

1. 緒 論

構造健全性評価を論じる上で，軸力と曲げを受ける片側き裂部材は典型的構造である．多くの場合，複雑なき裂付構造物もこの構造に代表させることができる．そのため，本構造に関する多くの破壊力学研究がなされてきた[1)~9)]．低強度のオーステナイト系ステンレス鋼き裂部材の強度については，き裂を有する構造物であっても負荷の増加に伴い顕著な塑性変形を示し，リガメント部の塑性崩壊により最終破壊に到るものと考えられる．したがって，低強度材料では軸力と曲げを受ける片側き裂部材の塑性崩壊強度を精度よく求めることが構造健全性評価上重要となる．従来の研究では限界荷重解析に基づき，当該構造に関する塑性崩壊荷重の上界および下界が求められてきた[1)~5)]．しかし，この塑性崩壊荷重に及ぼす負荷履歴の影響については，ハードウエアの問題から解明がされておらず，設計荷重に安全裕度をとることで回避してきていた．著者らはこれに対して，負荷履歴を考慮した形での塑性崩壊荷重評価が可能な不静定破壊力学実験装置を開発し一連の試験研究を行ってきた[10),11)]．

本研究では SUS316 鋼片側切欠付平板試験片に対して行った塑性崩壊実験に光弾性皮膜法を適用した．リガメント部の光弾性縞の観察を通じて，軸力と曲げを受ける片側切欠部材の塑性崩壊に到る塑性域の成長過程を調べた．その結果に基づき，本部材の塑性崩壊挙動に関する実験力学的考察を行う．

原稿受付 2003年9月16日

* 正会員 小山工業高等専門学校(〒323-0806 栃木県小山市大字中久喜 771)
** 群馬大学工学部(〒370-8515 群馬県桐生市天神町 1-5-1)
*** 正会員 小山工業高等専門学校名誉教授(〒306-0806 茨城県古河市緑町 21-4)

2. 実験方法

2. 1 実験装置および供試材料

塑性崩壊実験に用いた不静定破壊力学試験装置の概要を Fig. 1 に示す．本試験装置は軸力を負荷するための水平方向アクチュエーターと4点曲げ形式で曲げを負荷するための垂直方向アクチュエーターを独立して制御することが可能である．これにより，軸力・曲げ同時負荷および軸力と曲げの負荷順序を変えて実験を行うことができる．本実験装置の詳細については既報を参照されたい．

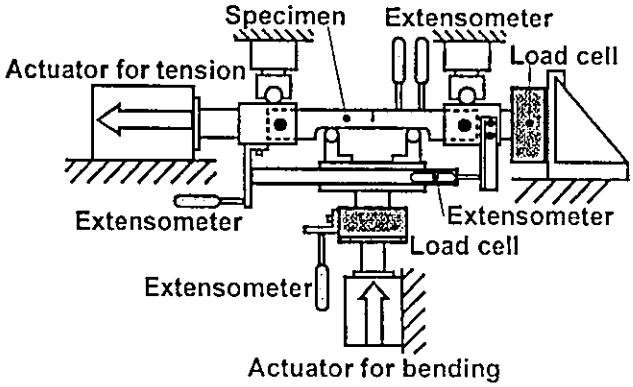

Fig.1　Load equipment part of the testing machine

供試材料はオーステナイト系ステンレス鋼 SUS316 であり，その化学成分を Table 1，室温における機械的性質を Table 2 にそれぞれ示す．Fig. 2 は試験片形状を示す．片側切欠はワイヤカット放電で加工し，その切欠底半径は 0. 16mm となっている．試験片板幅に対する深さの比は 0. 6 である．軸力の荷重線とリガメント中心を一致させた．この一致により軸力による曲げモーメントの発生を抑え，軸力の割合が大きい領域での試験を可能とした．

Table 1 Chemical composition of the material tested (wt.%)

C	Si	Mn	P	S	Ni	Cr	Mo
0. 05	0. 46	1. 38	0. 37	0. 003	10. 1	16. 4	2. 04

Table 2 Mechanical properties of the material tested

Yield stress MPa	Tensile stress MPa	Elongation %	Reduction of Area %
272	553	56	68

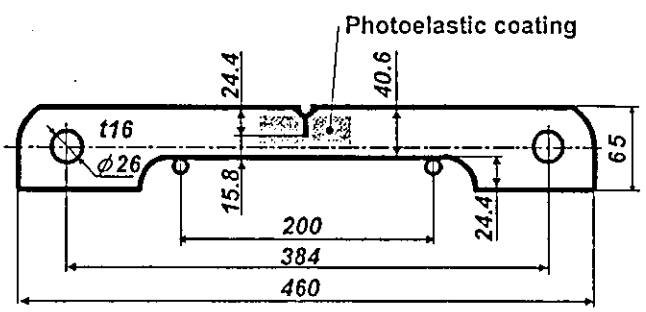

Fig. 2 Geometric figure of the specimen

2．2　光弾性皮膜実験用材料

光弾性皮膜は常温硬化型エポキシ樹脂エピコートに軟化材チオコールを混合したもので，これに硬化剤であるジエチルトリアミンを加えている．その共重合比は，エピコート：チオコール：ジエチルトリアミン＝10：10：1 である．作成した厚さ約２mmの光弾性皮膜を上記配合の原材料を用いてエメリーペーパーで仕上げた試験片リガメント部表面に接着した．

リガメント部表面に貼り付けた光弾性皮膜の等色線を観察するため，Fig.3 に示す水銀灯を光源とする反射型光弾性試験装置を用いた．試験の進行に伴う光弾性縞の変化状況をデジタルビデオカメラで撮影し，記録した．

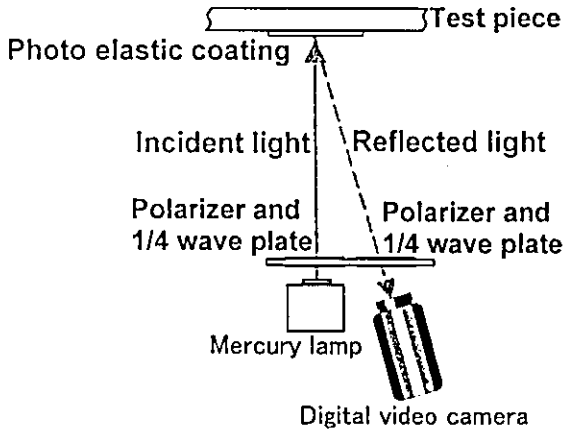

Fig.3　Schematic illustration of photoelastic coating technique

2．3　リガメント部応力算出方法

崩壊点付近では試験片の変形が進みたわみ角が大きくなるため，軸力の荷重線とリガメント中心がずれことになる．よって，軸力による比較的大きな負の曲げモーメントが発生する．Fig.4 はこの状況をモデル化して示したものである．ここで，b ：試験前の内側2本のピン間距離を，L ：試験前の外側2本のピン間距離を，ΔL ：曲げ変形によるピン間距離の変化および θ ：たわみ角（試験片上部の2点の垂直方向変位の計測結果から評価）とする．ピン間距離の変化による曲げモーメントの変化およびたわみ変形に起因する軸力による負の曲げモーメントを考慮した試験片に作用する曲げモーメント M_{total} は次式で与えられる．

$$M_{total} = \frac{W(L+\Delta L-b)}{4} - \frac{F(L+\Delta L)\tan\theta}{2} \qquad (1)$$

崩壊荷重は膜応力強さ P_m ´および曲げ応力強さ P_b ´

$$\left.\begin{aligned} P_m' &= F/BW' \\ P_b' &= 6M/BW'^2 \end{aligned}\right\} \qquad (2)$$

を用いて表示する．ここで，M: リガメント中心に関するモーメント，F: 軸力，B: 板厚および W': 試験片のリガメント幅である．M の評価には式(1)で与えられる M_{total}を用いた．

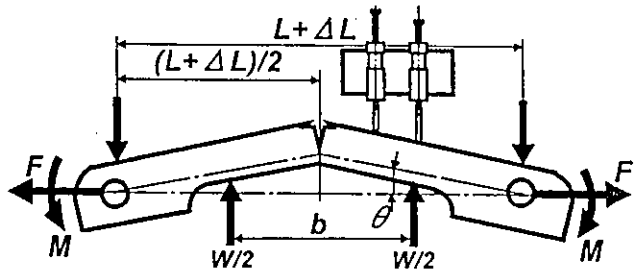

Fig. 4 Angular deflection of specimen

3．実験結果および考察

3．1 光弾性皮膜の光弾性感度

引張試験により得られた供試材料の応力－ひずみ線図を Fig. 5 に示す．

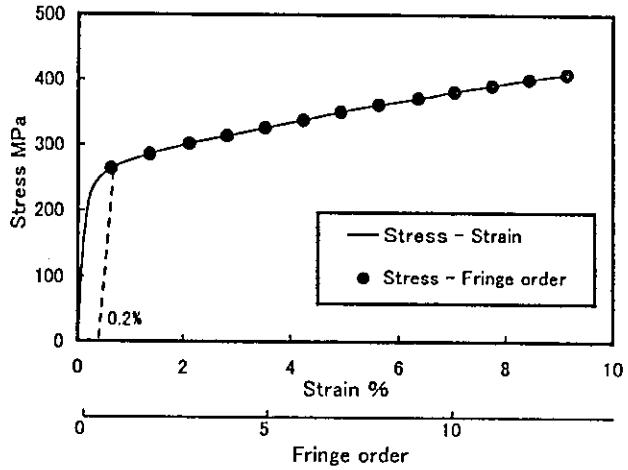

Fig. 5 Stress-strain curve of tested material and strain-optic law of a photoelasticity film

同図に応力－光弾性縞次数の関係を●で併せて示す．図に示すように，応力値が0．2 %耐力に達したとき1次の光弾性縞が発生するように皮膜材料を調整した．2次以降の縞は塑性領域で発生することになるが，1次の縞は弾性限度付近で発生する．したがって，供試材料の主応力差 $\sigma_1-\sigma_2$と最大せん断応力 τ_{max}との関係が

$$\sigma_1-\sigma_2=2\tau_{max} \tag{3}$$

で1次の縞についてはほぼ与えられる．いま主応力差が降伏応力 σ_yと等しいことから，1次の縞は

$$\sigma_1-\sigma_2=2k \tag{4}$$

で与えられるTrescaの降伏条件を満たす降伏開始点(＝塑性域の始まり)を示すことになる．ここで，k: せん断降伏応力($\sigma_y=2k$)である．塑性崩壊の定義は塑性域が全断面を貫通して塑性ヒンジを形成し，当該断面が塑性的にしか負荷に耐えられなくなることである．本研究での塑性崩壊は後述するように，切欠先端部で発生した1次の光弾性縞がリガメント背面に到達した時点として定義できる．参考までに次式で与えられる光弾性皮膜のひずみ差感度 βは

$$\beta=\frac{N}{d(\varepsilon_1-\varepsilon_2)} \tag{5}$$

28[1/mm]となった．ここで，N:光弾性縞次数，$\varepsilon_1-\varepsilon_2$:供試材料の主ひずみ差(＝$(1+\nu)\varepsilon_1$)，$\varepsilon_1$:単軸引張における主ひずみ，$\nu$:ポアソン比(= 0.5)，および d:光路程(= $2t$)，t:光弾性皮膜厚さである．

3．2 光弾性縞の観察

観察した光弾性縞のうち，塑性域がリガメント部を貫通した時点での代表的な3パターンを Fig.6 に示す．(a)は曲げのみを負荷した場合である．この場合にはリガメント背面からすべり変形による光弾性縞(圧縮成分)が同時に発生し，切欠側から発生した1次の光弾性縞との連結によって塑性崩壊が達成される．純曲げの場合についてはこの点を考慮して塑性崩壊途中での光弾性縞写真も示す．(b)は軸力・曲げを同時負荷した場合であり，(C)は軸力のみを負荷した場合である．図中に破線で示してあるのは1次の縞のループのリガメント方向先端位置の軌跡である．

Fig.7に片側き裂あるいは片側切欠に対してこれまでに仮定された上界解を与えるすべり線場を示す．(a)は純曲げに対する Green のすべり線場[12]，(b)は軸力・曲げが作用した場合の Rice のすべり線場[13]および(c)は純引張の場合の Hundy のすべり線場[14]である．Fig.6と Fig.7を比較すると，1次の縞のリガメント方向先端位置の軌跡は従来仮定されてきたすべり線場のすべり線と形状的に一致することがわかる．これより剛完全塑性体を仮定して与えられていたすべり線の形状は，実際の弾塑性体においては塑性域成長方向の先端部が描く軌跡に相当することがわかった．

3．3 塑性崩壊限度線図上での塑性崩壊パターンの表示

Fig. 8は塑性崩壊限度線図上に3．2で述べた塑性崩壊パターンの領域を示したものである．代表的な塑性崩壊パターンでの光弾性縞写真も併せて示す．図において，縦軸は曲げに対する塑性拘束係数 $P_b'/1.5\sigma_y$および横軸は引張に対する塑性拘束係数 P_m'/σ_yである．図中のプロットは不静定破壊力学実験装置を用いて評価した崩壊点を示す．

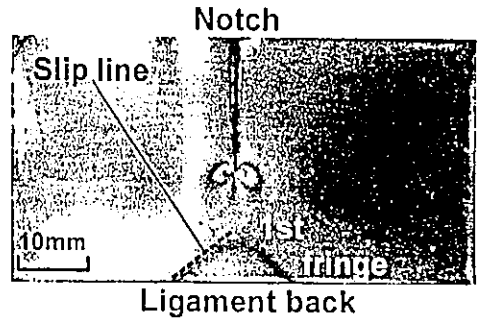

P_m'= 0*MPa*
P_b'= 518*MPa*

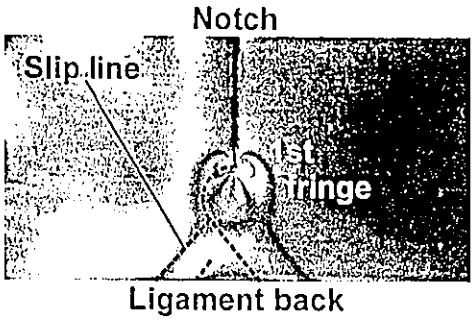

P_m'= 0*MPa*
P_b'= 558*MPa*

(a)　Pure bending

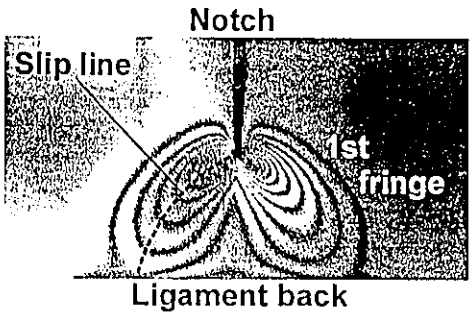

P_m'= 319*MPa*
P_b'= 352*MPa*

(b)　Tension+bending

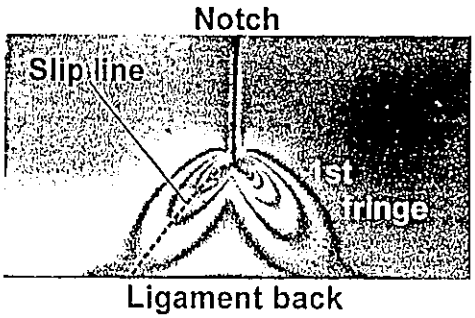

P_m'= 307*MPa*
P_b'= 0*MPa*

(c)　Pure tension

Fig. 6　Isochromatic fringes in the ligament part

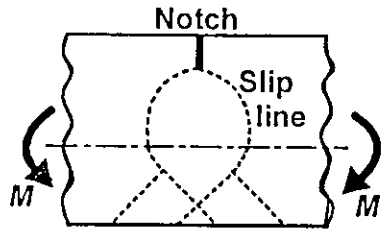

(a)　Green type

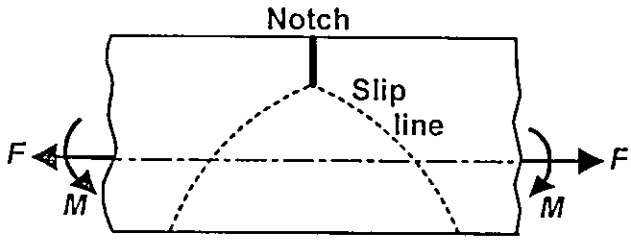

(b)　Rice type

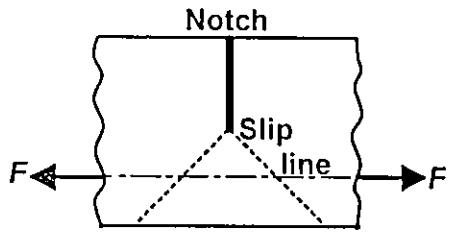

(c)　Hundy type

Fig.7　Slip line field

●は軸力・曲げ同時負荷の場合，▲は軸力負荷後曲げ負荷の場合および■は曲げ負荷後軸力負荷の場合をそれぞれ示す．崩壊点は前述の如く，1次の光弾性縞の先端がリガメント背面に達した時点，即ち本来の物理的塑性崩壊の定義であるリガメント部の塑性域貫通時点とした．その時点での式(1)および(2)で与えられる軸力および曲げモーメントによりそれぞれの塑性拘束係数を評価している．図中には軸力と曲げを受ける片側き裂部材の崩壊荷重の上界解も示してある．この上界解はP_m'/σ_y=0.551まではGreen[12]による純曲げの解を拡張して求めたものであり，それ以上のP_m'/σ_yではRiceら[13]による上界解となっている．図に示したように崩壊パターンを見ると負荷履歴に関係なく，P_m'/σ_y=0.551まではGreenのすべり線場を，それ以上のP_m'/σ_yではRiceらのすべり線場をほぼ形成していることがわかる．ただしP_m'/σ_y=0.551近傍では，両者のすべり線場の中間的な崩壊パターンが見られる．また，純引張の場合にはHundyによる純引張の場合のすべり線場にかなり近いものとなっている．したがって，軸力と曲げを受ける片側切欠部材の崩壊荷重を軸力と曲げのそれぞれの塑性拘束係数で評価しプロットすると，プロットした位置で塑性崩壊パターンがほぼ決まることになる．以上の結果を総合すると，実験力学的には軸力と曲げを受ける片側切欠部材の崩壊荷重は負荷履歴に関係なく上界解に従うものと判断される．

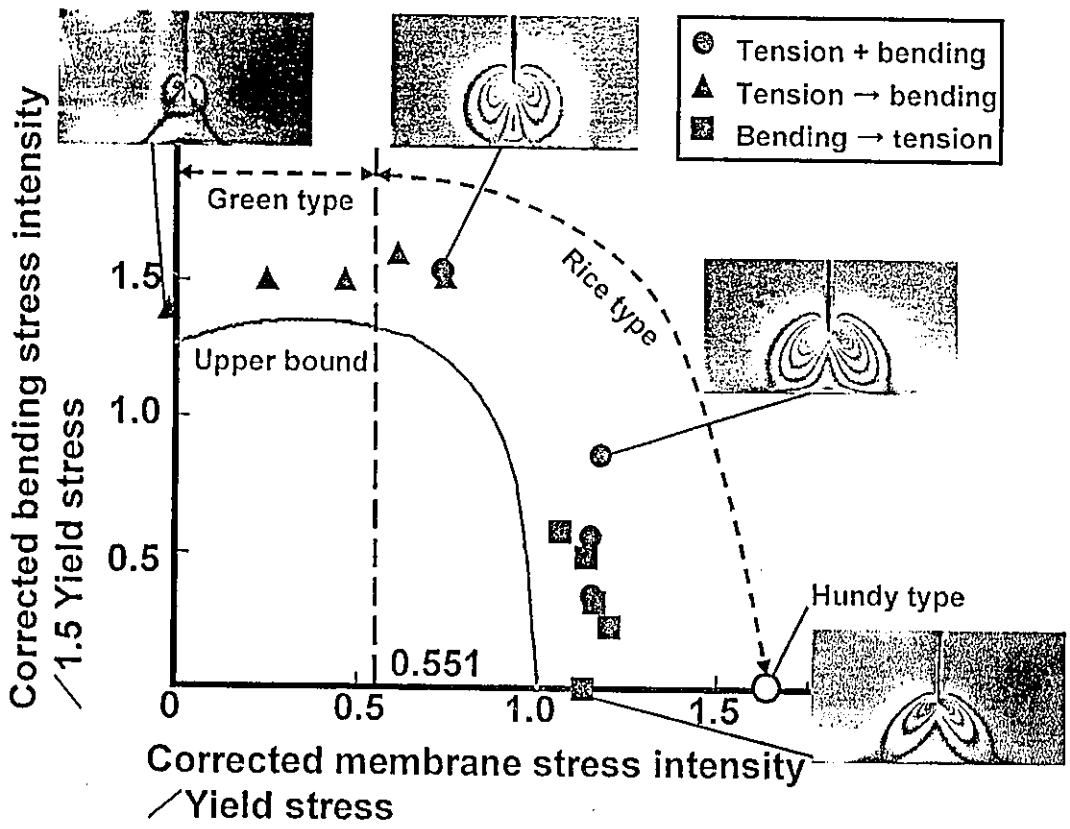

Fig.8 Distribution of plastic collapse point on the collapse limit chart

4. 結 論

軸力と曲げを受ける SUS316 鋼片側切欠部材の塑性崩壊荷重について，光弾性皮膜法を用いたリガメント部の光弾性縞観察を行い，実験力学的に考察した．得られた結論は以下の通り．

(1) 従来剛完全塑性体を仮定して与えられていた上界解を与えるすべり線場は，実際の弾塑性体においては塑性域成長方向の先端部が描く軌跡に相当する．

(2) 軸力と曲げを受ける片側切欠部材の崩壊荷重を軸力と曲げのそれぞれの塑性拘束係数で評価しプロットすると，プロットした位置で塑性崩壊パターン(上界解を与える Green タイプ，Rice タイプおよび Hundy タイプのいずれか)がほぼ決まる．

(3) 上記結論(1)および(2)より，実験力学的には軸力と曲げを受ける片側切欠部材の崩壊荷重は負荷履歴に関係なく上界解に従う．

本研究の一部は平成 11 年度笹川科学研究助成「垂直および水平荷重を受ける鉄鋼構造物の強度評価」および平成 14 年度から平成16年度までの3年計画で実施される厚生労働科学省科学研究費補助金「負荷履歴を考慮した経年圧力設備の高信頼度弾塑性破壊評価手法の開発」により実施したものであり，深謝致す次第である．

参 考 文 献

1) 岡村弘之，渡辺勝彦，高野太刀雄: コンプライアンス概念による線形破壊力学の拡張と応用，日本機械学会論文集，41-348 (1975), 2247-2254.

2) 白鳥正樹，三好俊郎，古矢正明: き裂材の塑性拘束に関する研究，日本機械学会論文集 (A 編)，47-423 (1977), 1139-1146.

3) 白鳥正樹，三好俊郎: SEN 試験片の塑性拘束係数と J 積分，日本機械学会論文集 (A 編)，46-407 (1980), 837-843.

4) 白鳥正樹，三好俊郎: 全面降伏した剛塑性体における COD と J 積分の関係，日本機械学会論文集 (A 編)，47-420 (1981), 800-809.

5) 三好俊郎，白鳥正樹: J 積分の板厚効果に関する一考察，日本機械学会論文集 (A 編)，47-423 (1981), 1136-1141.

6) 岡村弘之，高畑泰幸，影山和郎: 軸力と曲げを受けるき裂部材の崩壊荷重とその応用 (第 1 報)，日本機械学会論文集 (A 編)，49-445 (1983), 1076-1080.

7) 岡村弘之，高畑泰幸，影山和郎: 軸力と曲げを受けるき裂部材の崩壊荷重とその応用 (第 2 報)，日本機械学会論文集 (A 編)，49-445 (1983), 1081-1088.

8) 松原雅昭: 軸力と曲げを受ける片側き裂部材への不静定弾塑性破壊力学の適用, 日本機械学会論文集(A編), 56-526(1990), 1396-1399.

9) 松原雅昭: 軸力と曲げを受ける複数片側き裂を有する構造部材への不静定弾塑性破壊力学の適用, 日本機械学会論文集(A編), 57-534 (1991) , 281-284.

10) 伊澤 悟, 松原雅昭, 根津紀久雄, 坂本賢治, 近藤正幸, 太田敦士, 佐藤修一: 軸力と曲げを受けるSUS316鋼片側切欠部材の塑性崩壊評価, 日本機械学会2001年度年次大会講演論文集(I), (2001), 405-406.

11) 松原雅昭, 伊澤 悟, 平尾典盟, 壽島康二, 小山 哲, 町田康治, 川田大介, 坂本賢治, 根津紀久雄: 不静定破壊力学実験装置の開発, 日本機械学会論文集 (A編) , 67-659 (2001) , 1218 - 1222.

12) A. P. Green: The plastic yielding of notched bars due to bending, *Q. J. Mech. Appl. Math.*, 6(1953), 223-229.

13) James R. Rice: The line spring model for surface flows, *Proceedings of Surface Flaw Symposium, ASME Winter Annual Meeting*, (1972-11), 171-184.

14) B. B. Hundy: Plane plasticity, *Metallurgia*, 49(1954), 109-118.

The Effect of Heat Conduction on Stress Concentration Factors and Stress Intensity Factors Determined by Thermoelastic Stress Analyses

Takashi Honda[1], Tetsuya Sasaki[1], Teruhito Ohtsuka[2]
and Etsuji Yoshihisa[1]

1. Mechanical and System Safety Research Group, National Institute of Industrial Safety, Tokyo, Japan
2.Chemical Safety Research Group, National Institute of Industrial Safety, Tokyo, Japan

Abstract: The stress concentration factors and stress intensity factors evaluated by thermoelastic stress analysis method were lower than the comparable values calculated by the finite element method (FEM), and the error increased in proportion to those values regardless of the stress ratio.

In this study, the sources of the error between experimental results and numerical values were investigated in order to improve the accuracy of thermoelastic stress analyses. Since the major source was supposed to be the effect of heat conduction in specimens, the unsteady heat conduction analyses were conducted for three types of center holed specimens and center crack tension (CCT) specimens. According to the comparison between experimental results and numerical values, it was found that stress concentration factors were affected by heat conduction especially under 10Hz, but the errors of stress intensity factor were caused not by heat conduction but by the plastic zone size of a crack tip.

Key words: *Experimental stress analysis, Thermoelastic effect, Stress concentration, Stress intensity factor, Heat conduction,*

1. INTRODUCTION

The local stresses and strains near notches or cracks are very important for fracture analyses of cyclically loaded structural components. Thus, a number of experimental methods such as a photoelasticity method and numerical methods such as a finite element method have been developed to evaluate stresses and strains near notches or cracks. Among those methods, an thermoelastic stress analysis (TSA), which is relatively a new stress analysis technique based on the measurement of infrared radiation emitted from the surface of a body, can measure a two-dimensional stress distribution of real structure components without preparing special models like a photoelasticity method.

The authors applied this method to evaluate the stress concentration factors for several kind of notches and stress intensity factors for CT and CCT specimens in the previous study. However, the measured values were lower than the comparable values calculated by the FEM, and the error increased in proportion to those values regardless of the stress ratio[1].

The major source of the error was supposed to be the effect of heat conduction in a specimen. Thus, in this study, the effect of heat conduction in specimens was investigated by a finite differential analysis, and the results were compared with experimental results.

2. THERMOELASTIC STRESS ANALYSIS

2.1. Theory of TSA

Based on a theoretical treatment of the thermoelastic effect by Lord Kelvin [2], the temperature change associated with adiabatic elastic deformation in a body can be expressed in the form :

$$\Delta T = -\frac{E\alpha T}{\rho C_\varepsilon (1-2\nu)} \sum_{i=1}^{3} \Delta\varepsilon_{ii} = -K_m T \sum_{i=1}^{3} \Delta\sigma_{ii} \qquad (1)$$

where ΔT is change in temperature, E is the Young's modulus, α is the coefficient of linear thermal expansion, T is absolute temperature, ρ is the mass density, C_ε is the specific heat at constant strain, ν is the Poisson's ratio, $\Delta\varepsilon_{ii}$ is the normal strain change, K_m is the thermoelastic constant, $\Delta\sigma_{ii}$ is the sum of normal stress changes. Therefore, only the principal stress sum can be measured by an infrared stress analysis method.

2.2. Experimental Equipment

Figure 1 shows the schematic of the TSA system using in this study. Cyclic load is applied to the specimen by the servo-hydraulic fatigue machine. An infrared camera, of which sensitivity is 0.001 K corresponded to 1 MPa in steel, generates a signal in phase with the load signal in response to the infrared emission from the surface of a specimen. Since the temperature changes due to the thermoelastic effect are very small, the generated signals are averaged in the measurement time in order to improve the S/N ratio. The image of change in temperature ΔT is obtained by subtracting the temperature image in minimum load T_{min} from the one in maximum load T_{max}.

3. EXPERIMENTAL PROCEDURE

Three types of center holed specimen were prepared in this study. The material used in this study was JIS S45C steel. The mechanical and thermophysical properties of this material are shown in Table 1. The 3mm thick sheet specimens shown in Fig. 2 were machined from a 3.3mm thick sheet material. The proportion of diameter to width

Corresponding author:
T. Honda, honda@anken.go.jp

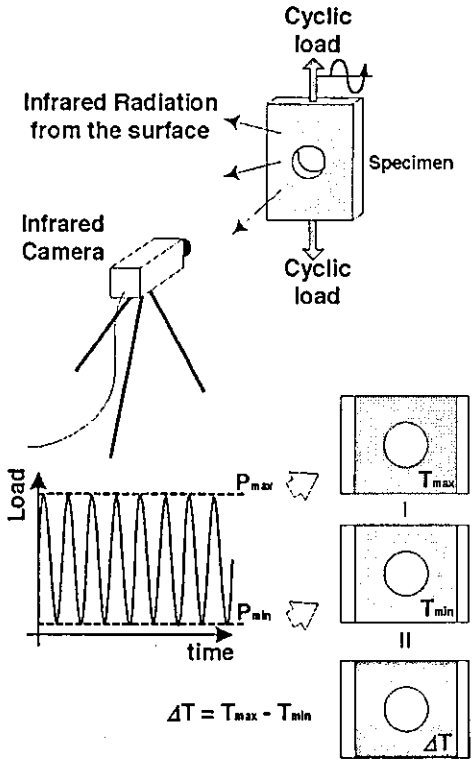

Fig.1. Schematic of the infrared stress analysis method.

was constant in all specimens in order to have the same stress concentration factor.

The configuration of CCT specimen used in this study is shown in Fig. 3. The material used for CCT specimen was JIS S45C steel, of which mechanical properties were the same with those of center holed specimens. The pre-cracks were introduced using the servo-hydraulic fatigue machine of 196 kN capacity until the crack length $2a$ became 20mm.

In order to investigate the effect of heat conduction in a specimen, each specimen was cyclically loaded at different levels of frequency of 1, 5, 10 and 15 Hz using the servo-hydraulic fatigue machine of 196 kN capacity. Prior to the stress measurement, all specimens were cleaned with acetone and then coated with matt black spray paint to maximize their emissivity. The stress measurement by thermoelastic technique was carried out using the infrared stress imaging system JTG8000 developed by JEOL.

4. UNSTEADY HEAT CONDUCTION ANALYSIS

The unsteady heat conduction analysis under cyclic loading was carried out by a finite differential method (FDM) in order to investigate the effect of the heat conduction in a specimen on measured values.

In case of isotropic material, the equation of two-dimensional unsteady heat conduction is:

$$\rho c\frac{\partial T}{\partial t}=\lambda\left(\frac{\partial^2 T}{\partial x^2}+\frac{\partial^2 T}{\partial y^2}\right)+\frac{dQ}{dt} \qquad (2)$$

where ρ is a density, c is a specific heat, T is temperature, λ is a thermal conductivity, Q is the quantity of heat supplied to unit volume. Also dQ is expressed by Eq.(1):

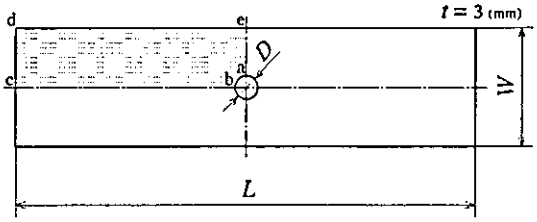

	L (mm)	W (mm)	D (mm)
Type A	250	30	6
Type B	250	50	10
Type C	400	100	20

Fig.2. Configuration of center hole specimens.

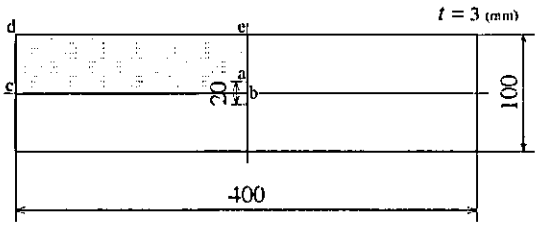

Fig.3. Configuration of CCT specimens.

Table 1. Mechanical properties of materials used.

	Yield Stress (MPa)	Tensile Strength (MPa)	Elongation (%)
S45C	450	550	30

Table 2. Boundary conditions in unsteady heat conduction analysis.

	Boundary condition
a - b	$-\lambda(\partial T/\partial n)=0$
b - c	$-\lambda(\partial T/\partial n)=0$
c - d - e	$T=T_c$
e - a	$-\lambda(\partial T/\partial n)=0$

$$dQ = Cv\,dT = -\rho c\,Km\,T\,d\sigma. \qquad (3)$$

Since specimens were loaded in sinusoidal waves in this study, the principal stress sum σ is given as follows:

$$\sigma=\sigma_a(x,y)\sin\omega t \qquad (4)$$

where ω is the frequency of cyclic load, t is time, $\sigma_a(x,y)$ is the stress amplitude at the point (x,y), which is determined by the finite element method (FEM). The unsteady heat conduction analyses were carried out by FDM using the forward difference equation of Eq.(2).

Considering the symmetrical configuration, one fourth of the specimens hatched in Fig. 2 and 3 were analyzed. The boundary conditions are given in Table 2. In this ta-

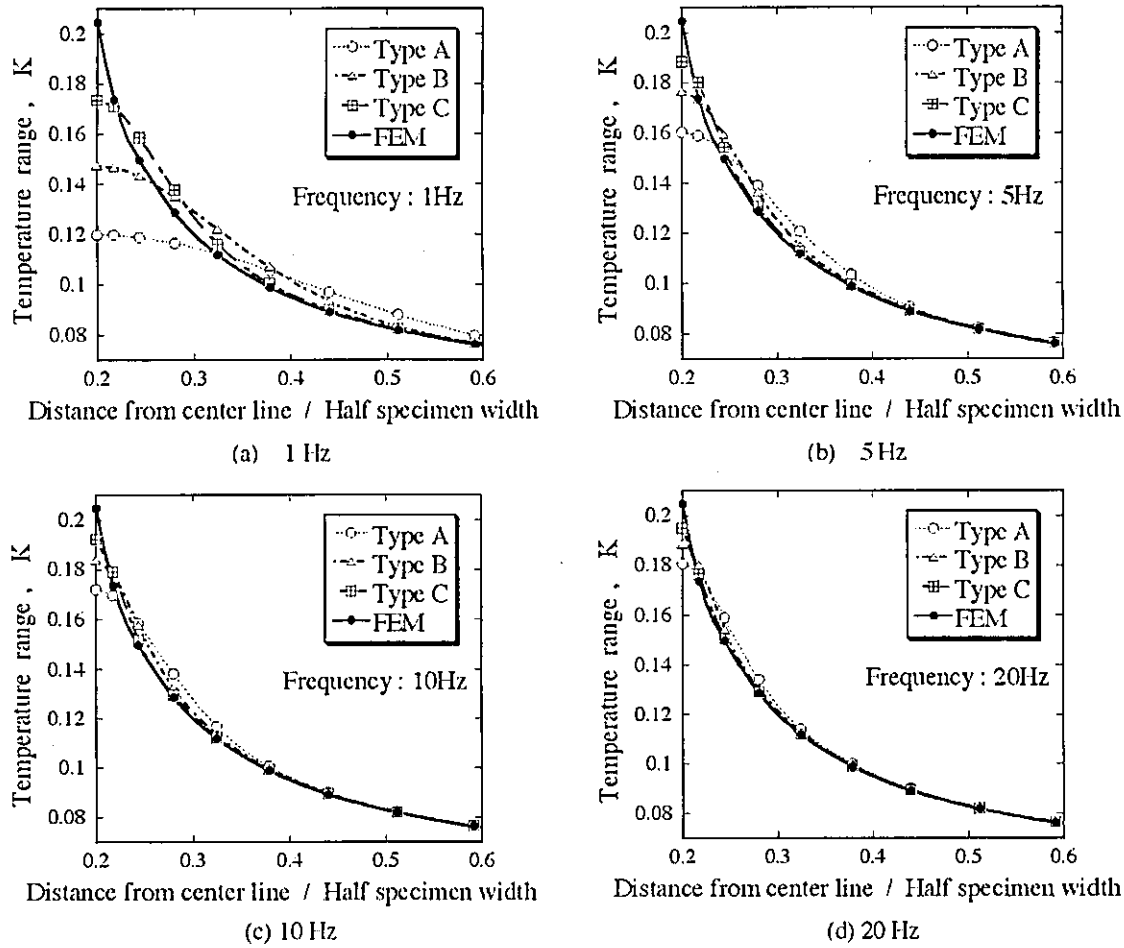

Fig.4. Distribution of the temperature range under cyclic loading in the minimum cross section. Applied stress range = 70 MPa.

ble, n is a normal vector for the boundary. The ambient temperature Te and the initial temperature of specimens were 293K, and time step Δt was 10^{-4}s.

5. RESULTS AND DISCUSSION

5.1. Effect of heat conduction on stress concentration factor

Prior to the unsteady heat conduction analysis, the stresses of the center holed specimens used in this study were analyzed by FEM under the plane stress condition using a two-dimensional mesh. The stress concentration factor K_t obtained from the analysis result was 2.53, which was similar to the strict solution 2.51[3]. Then, the temperature amplitude of each node was calculated from the FEM result using Eq.(1), and was substituted in Eq.(4). Accordingly, the unsteady heat conduction analyses by the FDM were carried out using the same mesh as FEM.

Figure 4 shows the results of FDM under cyclic loading in the minimum cross section. For the comparison among specimens, the abscissa of each graph is normalized by the half specimen width. The FEM results, which are temperature distributions in the perfect adiabatic condition, were also shown in this figure. As can be seen in this figure, it was found that the adiabatic condition of each specimen was achieved with the increase of the loading frequency. However, the temperature distributions were different among specimens at the same fre-

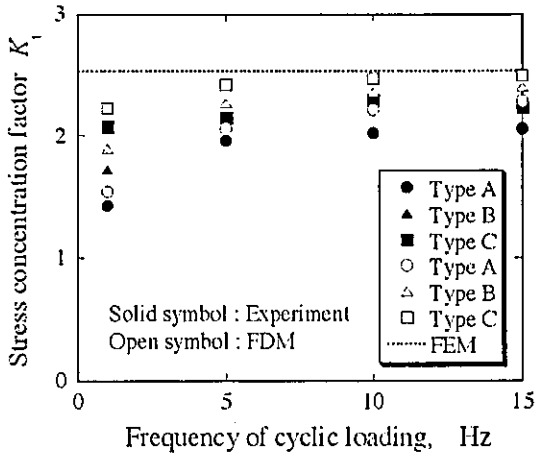

Fig.5. Relationship between K_t and the loading frequency.

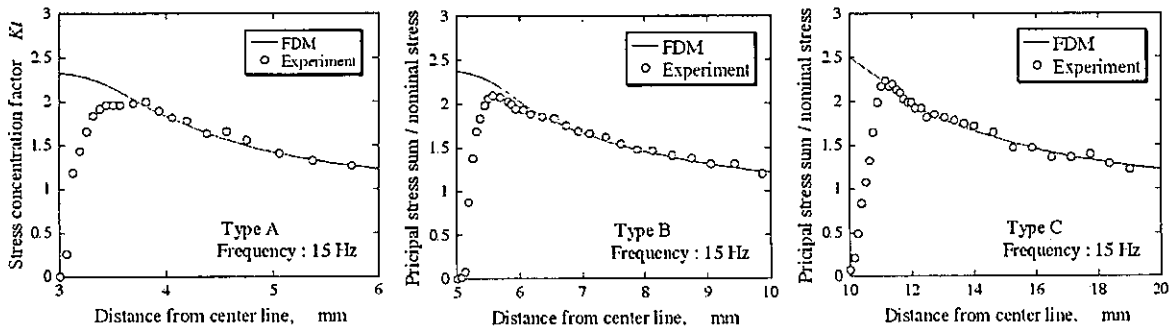

(a) Type A (b) Type B (c) Type C

Fig. 6. Comparison of stress distributions near the notch root between experimental results and FDM results at 15Hz.

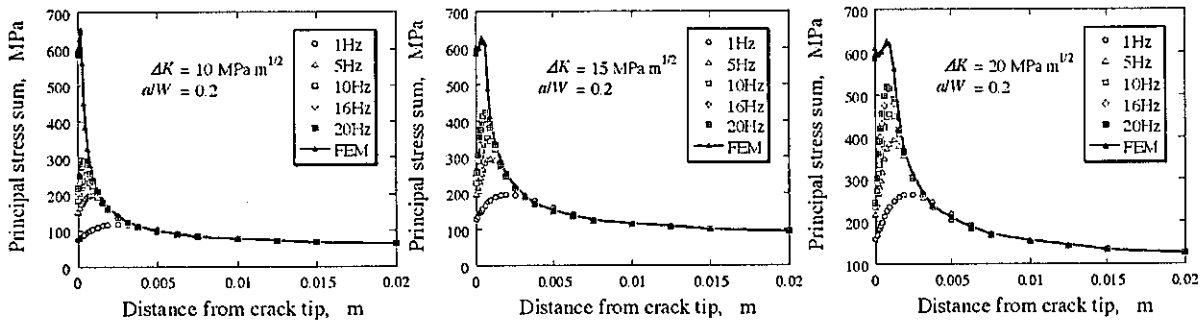

(a) $\Delta K = 10\ \mathrm{MPa \cdot m^{1/2}}$ (b) $\Delta K = 15\ \mathrm{MPa \cdot m^{1/2}}$ (c) $\Delta K = 20\ \mathrm{MPa \cdot m^{1/2}}$

Fig. 7. Distributions of the principal stress sum along the ligament of CCT specimen analyzed by FDM.

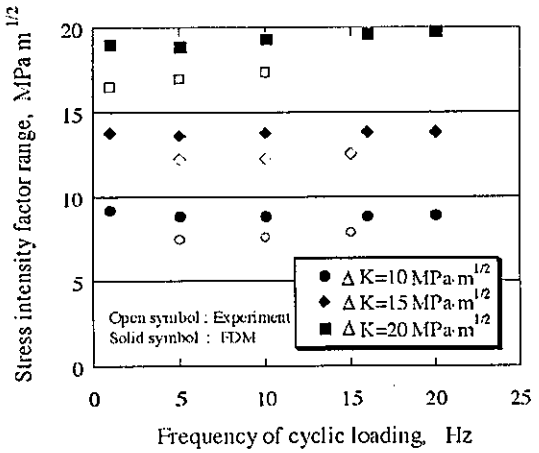

Fig. 8. Relationship between ΔK and the loading frequency.

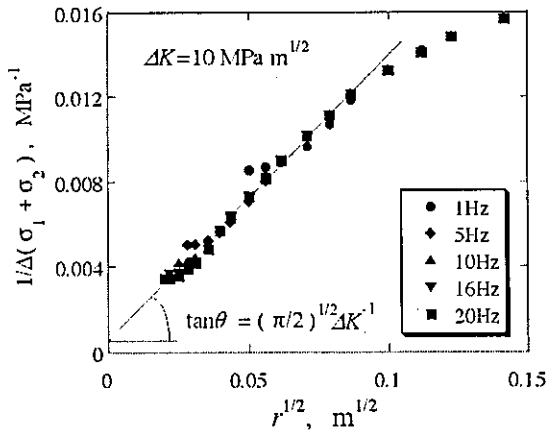

Fig. 9. Plot of $1/\Delta(\sigma_1+\sigma_2)$ vs $r^{1/2}$ for results of FDM.

quency and the difference was remarkable under 10Hz. It is quite common for researchers in this field that the apparent adiabatic condition is achieved at 5 – 10 Hz [4]. However, it is hard to say from this figure that the apparent adiabatic condition is achieved even at 10Hz.

Then, stress concentration factors K_t were calculated from the FDM results and compared with the measurement results. Here, K_t was defined as the ratio of the principal stress sum to nominal stress in the minimum cross section because only the principal stress sum can be measured by this measurement method basically. Fig. 5 shows the relationship between K_t and the loading frequency. FEM results are also shown in this figure. K_t values of all specimens for both FDM and the experiment increased with an increment of frequency of cyclic loading and saturated at about 10Hz. However, stress concentration factors obtained by experiments were smaller than those by FDM at all frequencies and the error was at most 10%.

In order to clarify the cause of the error, experimental values and analytic results were compared in detail. Fig. 6 shows the comparison of stress distributions near the notch root between experimental results and FDM results at 15Hz. As can be seen in this figure, experimental re-

sults of all specimens were agreed well with analytical results except for near the notch root and the maximum values of experimental results were appeared at the distance, about 1mm, from notch roots. Those phenomena are due to the edge effect of a infrared camera. Particularly, stress values of Type A specimen between about 3.3mm and 3.6mm from the center line were constant and did not agree with the analytical results in Fig. 6(a). This phenomenon occurred due to the fact that gradient of temperature near the notch root have exceeded the resolution limit of the infrared camera because these were not observed at frequencies less than 15Hz. Consequently, the experimental value of K_t become always smaller than the analytical value.

5.2. Effect of heat conduction on stress intensity factor range

The unsteady heat conduction analyses of CCT specimens under cyclic loading were carried out by FDM in order to investigate the effect of the heat conduction on stress intensity factor range ΔK. Since not σ but $\Delta\sigma$ is measured by TSA, ΔK can be obtained from a measurement result.

Figure 7 shows the distributions of the principal stress sum along the ligament of the CCT specimen analyzed by FDM. Also, FEM results are shown in this figure. As can be seen in this figure, it is clear that the stress distributions were affected by heat conduction in the specimen. Then stress intensity factor ranges ΔK were calculated by the extrapolation method often used in the photoelasticity method[5] and compared with experimental results. Fig. 8 shows the relationship between ΔK and the loading frequency. However, each value of ΔK was hardly affected by the loading frequency and practically constant. In case of obtaining ΔK by the extrapolation method, ΔK is decided from the gradient of the plots in Fig. 9. The accuracy of ΔK is greatly affected the stress values of crack vicinity. However, the stresses around crack tip can not be measured accurately by TSA due to plastic deformation and heat conduction. Accordingly, the value of stress intensity factor range was not affected by the load frequency.

Comparing between experimental values and analytical values in Fig. 8, the ΔK values of experiments were smaller than the values of FDM and the difference tended to increase in proportion to those values. The tendency seemed to be caused by the plastic zone size of a crack tip. As can be seen in Fig. 7, the maximum value of the principal stress sum appeared in the position away from the crack tip with the increase of ΔK. Consequently, it became difficult to identify the position of the crack tip from the measurement result. Therefore it is necessary to develop the method to identify the position of the crack tip from a stress image of TSA in order to improve the accuracy of ΔK.

6. CONCLUSIONS

In this paper, in order to improve the measurement accuracy of stress concentration factors and stress intensity factors by the thermoelastic stress analysis method, the cause of the error between measurement results and analytical values was clarified by means of the unsteady heat conduction analysis. The obtained results are summarized as follows:

(1) It is necessary to carry out the stress measurement at the frequency over 10Hz in case of steel using the thermoelastic stress analysis because the measurement result is greatly affected by heat conduction in a specimen.

(2) The decrease in the accuracy of measurement values also occurred due to the resolution limit of the infrared camera when the notch radius was 3mm.

(3) The errors of stress intensity factors between estimated values and analytical results were caused not by heat conduction but by the plastic deformation around crack tips.

REFERENCES

1. Y. Kitsunai, T. Honda, and T. Sasaki, Trans. Jpn. Soc. Mech. Eng., A-64 (1998), pp. 2782-2787 (in Japanese).
2. Y. C. Fing, Foundations of Solid Mechanics, Prentice Hall (1965).
3. M. Nishida, Stress Concentration, Morikita Shuppan (1967), pp.261 (in Japanese).
4. S. A. Dunn, Exp. Mech., March (1993), pp.32-36.
5. K. Kunio, H. Nakazawa, I. Hayashi and H. Okamura, The Experimental Method of Fracture Mechanics, Asakura Shoten (1984), pp.41 (in Japanese).